


## Superradiant Scattering by a Limit Cycle

Tiemo Pedergrana<sup>✉\*</sup> and Nicolas Noiray<sup>✉†</sup>

*CAPS Laboratory, Department of Mechanical and Process Engineering, ETH Zürich, Sonneggstrasse 3, Zürich 8092, Switzerland*

 (Received 16 May 2023; revised 5 August 2023; accepted 22 August 2023; published 28 September 2023)

Interference with a nonlinear cavity mode undergoing a self-sustained limit cycle can lead to superradiant amplification of incident waves. This effect, which results from nonlinear wave-mode coupling, is theoretically predicted and experimentally confirmed in this work. On the theoretical side, we present a nonlinear coupled-mode framework to derive an analytical expression for the scattering matrix. These predictions are then validated against experiments on a superradiant acoustic meta-atom, which uses deep-cavity whistling to create a limit cycle. The proposed all-acoustic meta-atom requires no active elements to manipulate the sound field, but achieves superradiant amplification by nonreciprocal coupling between the incident wave and the synchronized whistling tone (limit cycle). We demonstrate with this setup that the nonlinear phenomena we present can be exploited to quasipassively tune the scattering matrix of a resonant cavity. As a proof of concept, we convert a lossy, weakly reflective scatterer into a reflection amplifier. We explain how the synchronization-based realization of superradiance reported in this work may be exploited in the future to design lossless, nonacoustic scatterers for metamaterial applications.

DOI: [10.1103/PhysRevApplied.20.034068](https://doi.org/10.1103/PhysRevApplied.20.034068)

### I. INTRODUCTION

Superradiance occurs when an energetic, radiating region scatters incident waves with a net amplification [1–3]. Paradigmatic manifestations are the Penrose process, by which particles gain momentum from a rotating black hole [4–7] and the Zel’dovich mechanism, where a rotating metallic cylinder increases electromagnetic oscillations [8]. Superradiant scattering has been realized with analogue black holes [9–12], in Bose-Einstein condensates and quantum vortices [13–17], and using orbital angular-momentum beams [18,19]. Discussions of superradiance in the context of stars can be found in Refs. [20–23]. Extraction of energy from rotating systems has been investigated in optics [24,25], acoustics [26], hydrodynamics [27,28], and quantum mechanics [29–31].

Here, we consider a scenario where superradiant scattering is achieved in a one-dimensional (1D) waveguide by scattering harmonic waves at a self-oscillating cavity mode  $a$ . The dynamics of  $a$  in the absence of incident waves are governed by a nonlinear damping force  $F_d$ , leading to a

stable limit cycle  $a_0 = |a_0| e^{i\omega_0 t}$  at the self-sustained angular frequency  $\omega_0 = 2\pi f_0$ . If a wave with frequency  $f \approx f_0$  impinges on the cavity, nonlinear wave-mode coupling takes place, resulting in an amplitude-dependent scattering matrix. We show that, in this scenario, the incident waves can extract energy by interfering with the synchronized limit cycle, and that the entries of  $S$  may be tuned by varying the incident wave amplitude. We demonstrate that this nonlinear interference leads to one-way superradiant amplification while simultaneously improving the isolation of the other direction. The reader is referred to Fig. 1 for a sketch of this concept.

To model the wave-mode coupling described above, a nonlinear extension of temporal coupled-mode theory (TCMT) is proposed. TCMT describes unitary multiport scattering by linearly stable resonant cavities [32–36]. In contrast, here, we are interested in modeling *nonlinear* scattering by cavities exhibiting a self-oscillating limit cycle. Despite fruitful recent applications of coupled-mode theories in optics [37–40], electrodynamics [41,42], quantum mechanics [43–45], and acoustics [46–48], no analogous, *generic* framework exists for nonlinear systems. The present work aims to fill this gap in the literature by extending TCMT to nonlinearities and deriving the scattering matrix in this general case.

The proposed nonlinear framework can be adjusted to a given experimental setting. We sketch in Sec. II how this method can be applied to model general multidimensional scattering problems. For simplicity, throughout the rest of the work, we restrict our discussion to the case of a single

\*ptiemo@ethz.ch

†noirayn@ethz.ch

*Published by the American Physical Society under the terms of the [Creative Commons Attribution 4.0 International](https://creativecommons.org/licenses/by/4.0/) license. Further distribution of this work must maintain attribution to the author(s) and the published article’s title, journal citation, and DOI.*

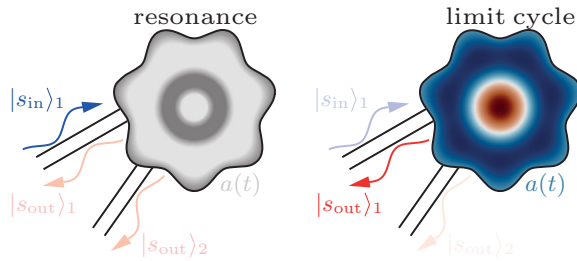


FIG. 1. In a lossy resonant cavity with multiple ports, due to dissipative effects, the energy of the incident waves  $\langle s_{in} | s_{in} \rangle$  always exceeds that of the outgoing waves  $\langle s_{out} | s_{out} \rangle$  (left inset). We show that this fundamental limitation can be overcome by inducing a self-sustained limit cycle in the cavity to enable superradiant scattering. This effect is based on the synchronization of the limit cycle with the incident waves, and allows for one-way amplification of the outgoing waves, while simultaneously improving isolation in the other direction. We present theoretical results, which explain this mechanism and validate them against nonlinear scattering experiments on a superradiant acoustic meta-atom with two ports.

limit cycle in a cavity with two ports. This approximation is valid when a single mode dominates the spectrum, which is the case in our experiments. More specifically, we consider an asymmetric, superradiant reflection amplifier coupled to a 1D waveguide. The choice of modeling of a reflective system is motivated by our experimental setup, in which scattering at the eigenfrequency of the limit cycle is characterized by large reflection and low transmission. Realizing the transmissive, weakly reflective counterpart to this 1D configuration, as well as developing higher-dimensional scatterers encompassing more participating modes and more ports, is part of our ongoing research. The theoretical model we present emulates our experiments with remarkable accuracy using only few parameters, whose numerical values were set manually to match the experiments, in order to facilitate comparison of the results. No fit was performed, although this could be done in the future. Besides the model’s quantitative, descriptive capabilities, it accurately predicts the overall nonlinear scattering behavior of a cavity-based limit cycle that would be expected in real-world experiments. The latter, qualitative feature is emphasized in this study.

In our setup, a limit cycle is realized through a type of aeroacoustic instability called “deep-cavity whistling” [49–51] that has recently been revisited both theoretically and experimentally [52–54]. Simply put, when a low-Mach air flow grazes over a (deep) cavity’s aperture at the right angle and velocity, it can destabilize one of its resonant modes, which leads to self-sustained oscillations (whistling). This transition from resonance to whistling, which can be modeled as the supercritical Hopf bifurcation associated with a Stuart-Landau oscillator [53,55–57], is

exploited in this work to create a self-sustained limit cycle in the cavity.

A benefit of such an aeroacoustic setup is that when the air flow is turned off, the cavity has a resonance at  $f_0$  and when it is turned on, the cavity has a limit cycle close to the same frequency. This insensitivity of the eigenfrequency to the aeroacoustic instability allows for a side-by-side comparison of resonance-based and limit-cycle-enhanced scattering. Before presenting our experiments, however, we first take a step back from the acoustic realm to derive a generic coupled-mode framework for the nonlinear scattering matrix. In doing so, we make an argument that the phenomena we discuss in this work are not restricted to any particular physical theory, such as acoustics or electromagnetics, but can generically arise from the dynamic, nonreciprocal coupling between a limit cycle and waves interfering with it.

## II. THEORETICAL MODEL

The linear-cubic damping force  $F_d = (-\gamma + \beta - \kappa|a|^2)a$  of the Stuart-Landau oscillator governs a stable limit cycle arising from a supercritical Hopf bifurcation (for  $\beta > \gamma$ ), and predicts an unbounded effective resistance  $-F_d/a$  as the amplitude  $|a|$  goes to infinity. Experiments [53, Fig. 8] and numerical simulations [58] on whistling configurations similar to the one used in this work showed that the resistance of the cavity-waveguide interface in the presence of mean flow, which can take negative values when the aeroacoustic feedback is constructive, exhibits a sigmoid-type behavior with respect to the forcing amplitude as its value tends towards the positive constant resistance measured in the absence of flow. This saturated and *finite* positive resistance corresponds to a resonant scattering process when the forcing amplitude is sufficiently large. In this work, to be consistent with these experimental observations, we envision a damping nonlinearity, which is quasiequivalent to the Stuart-Landau model in the vicinity of the origin and near the limit cycle, but with a finite resistance at large amplitudes (see Fig. 2):

$$F_d(a) = \left( -\gamma + \frac{\beta}{1 + \kappa|a|^2} \right) a. \quad (1)$$

In accordance with the above considerations, the following set of equations, including a nonlinear damping force  $F_d$ , wave-to-mode coupling, wave-to-wave coupling, and mode-to-wave coupling, is used to model the nonlinear scattering process:

$$\dot{a} = i\omega_0 a - \gamma a + \frac{\beta a}{1 + \kappa|a|^2} + D^\dagger |s_{in}\rangle, \quad (2)$$

$$|s_{out}\rangle = C |s_{in}\rangle + Da. \quad (3)$$

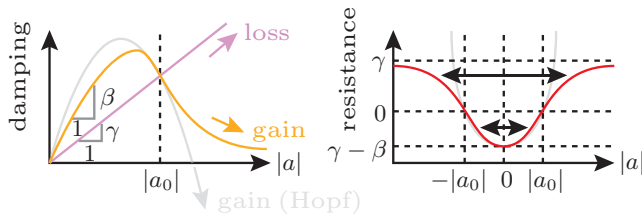


FIG. 2. Damping nonlinearity envisioned in this work (not to scale). Shown are the loss and gain components of the nonlinear damping force  $F_d$  (left inset) and the effective resistance  $-F_d/a$  (right inset). When the linear gain coefficient  $\beta$  exceeds the damping constant  $\gamma$ , a stable limit cycle occurs at  $a = a_0$ . The nonlinear gain and resistance curves of a Stuart-Landau oscillator describing a supercritical Hopf bifurcation are shown in gray.

In this model,  $a$  is the complex modal amplitude, the dot represents differentiation with respect to time  $t \in \mathbb{R}^+$ ,  $i$  is the imaginary unit,  $\omega_0 = 2\pi f_0 \in \mathbb{R}^+$  is the eigenfrequency,  $\gamma \in \mathbb{R}^+$  is the damping constant,  $\beta \in \mathbb{R}^+$  is the linear gain coefficient,  $\kappa \in \mathbb{R}^+$  is the nonlinearity constant, the dagger  $\dagger$  symbolizes the Hermitian conjugate and  $|s_{\text{in}}\rangle, |s_{\text{out}}\rangle \in \mathbb{C}^2$  are the incident and outgoing waves at the forcing frequency  $\omega = 2\pi f \in \mathbb{R}^+$ . As is customary in the TCMT literature, we use bra-ket notation [59] for the waves. Since we are dealing with a finite-dimensional complex vector space, a ket  $|s\rangle$  denotes a complex column vector, whose Hermitian conjugate is given by the bra  $\langle s| = |s\rangle^\dagger$ . Accordingly,  $\langle s|s\rangle$  denotes the squared magnitude of  $|s\rangle$ . The matrix  $D \in \mathbb{R}^2$  defines the nonreciprocal coupling between the nonlinear mode  $a$  and  $|s_{\text{in}}\rangle$ . We call  $D$  a matrix, although, here, it is a vector. In a general  $n$ -port scattering configuration involving  $m$  modes,  $D$  is a complex  $n$ -by- $m$  matrix.  $C \in \mathbb{R}^{2 \times 2}$  is the background scattering matrix. Self-oscillation can occur only for  $\beta > \gamma$ , which is the case considered here. The specific form of the nonlinear damping force Eq. (1), which uses a rational function in  $|a|$  to represent the gain saturation at large amplitudes, was chosen because it leads to an analytically tractable system. In principle, any nonlinearity resulting in qualitatively similar resistance and gain curves as those sketched in Fig. 2 could be used. It is worth noting that the coupling matrix  $D$  is not independent of the damping constant  $\gamma$ . We show below how  $D$  is related to the partition of the damping  $\gamma = \gamma_r + \gamma_i$  into reversible radiation losses ( $\gamma_r$ ) through the ports and irreversible losses in the cavity ( $\gamma_i$ ), which, in the present acoustic meta-atom, are due to viscothermal dissipation.

In the absence of forcing, the modal dynamics Eq. (2) describe a limit cycle with frequency  $f_0$  and constant amplitude  $|a_0| = \sqrt{(\beta/\gamma - 1)/\kappa}$ . It is straightforward to verify that this limit cycle is linearly stable for  $\beta > \gamma$  and that the origin is unstable in this case. Conversely, for  $\beta < \gamma$ , the limit cycle does not exist and the origin is stable. At large amplitudes ( $|a| \gg |a_0|$ ), the linear damping  $-\gamma a$

dominates the nonlinear,  $\beta$ -modulated term in Eq. (2). In this limit, therefore, the dynamics (2) reduce to the classic TCMT equations

$$\dot{a} = (i\omega_0 - \gamma)a + D^\dagger |s_{\text{in}}\rangle, \quad (4)$$

$$|s_{\text{out}}\rangle = C|s_{\text{in}}\rangle + Da, \quad (5)$$

which are described by the linear scattering matrix

$$S_{\text{TCMT}} = C + DF^{-1}D^\dagger, \quad (6)$$

where  $F = i(\omega - \omega_0) + \gamma$ .

In this work, to create a limit cycle, we impose an air flow in the waveguide to which the cavity is attached. The small, but non-negligible Mach number  $\text{Ma} \approx 0.17$  of this air flow induces a bias in the scattering matrix. To model this asymmetry, we construct the coupling matrix  $D$  from two *a priori* defined quantities: the target matrix  $S_*$  corresponding to resonant scattering at large amplitudes and the background matrix  $C$ , which describes scattering in the waveguide when it is decoupled from the cavity.  $C$  is determined by the nonresonant nature of a given scattering configuration when the cavity is decoupled from the waveguide. In turn,  $S_*$  describes the desired, optimal scattering state at the combined waveguide-cavity system.

We now sketch how the coupling matrix  $D$  can be derived, given  $S_*$  and  $C$ , for a general scatterer with  $n$  ports and  $m$  active modes, whose dynamics are, respectively, described by linear systems of the form Eqs. (4) and (5). For simplicity, we assume (a)  $n > m$  (more ports than modes) and (b) that there exists a subset of  $m$  eigenvalues of the  $n$ -by- $n$  matrix  $S_* - C$  whose magnitudes exceed those of the remaining eigenvalues. Under these assumptions,  $D$  can be derived along the following lines.

(1) Compute the eigenspectrum  $\{\lambda_j, v_j\}, j = 1, \dots, n$  of the  $n$ -by- $n$  matrix  $S_* - C$ .

(2) Select the dominant  $m$ -dimensional subspectrum, defined by the set of eigenvalues  $\lambda_j, j = 1, \dots, m$  with the largest magnitude and their corresponding eigenvectors  $v_j$ .

(3) Approximate  $S_* - C \approx \sum_j^m b_j \lambda_j v_j^\dagger v_j$  with suitably chosen coefficients  $b_j$  and compare with Eq. (6) to derive  $D$ .

In the 1D problem considered here,  $m = 1$  and  $b_1 = 1$ . It is part of our ongoing research to demonstrate on specific examples how the above pseudoalgorithm can be used to derive the coupling matrix  $D$  for higher-dimensional scattering systems ( $n > 2, m > 1$ ). It is worth noting that the method for deriving  $D$  sketched above is based on a (set of) linear system(s) in the form of Eqs. (4) and (5). For the damping force in Eq. (1) considered in this work, this linear system exists as a well-defined limit ( $|a| \rightarrow \infty$ ) of the nonlinear system given by Eqs. (2) and (3), see also Fig. 2.

Should the above steps be applied to a scatterer with a different type of nonlinearity than what is considered here, then it would be advantageous if there also existed some limit of that system in which it becomes linear. Rewriting this linear limit in the canonical TCMT form described by Eqs. (4) and (5), one can follow the above steps to derive  $D$ . Nonlinearities in the wave-mode coupling matrix  $D$  itself are neglected here, but could be considered in the future.

For brevity, the full derivation of the scattering matrix is given in Appendix A and only the main steps are reported here. We follow the convention by which the diagonal and off-diagonal elements of  $S$  are reflection and transmission coefficients, respectively [60]. For clarity, we define the amplitude reflection and transmission coefficients as  $\mathcal{R}_{j \rightarrow j} = |S_{jj}|$  and  $\mathcal{T}_{j \rightarrow k} = |S_{jk}|$ ,  $j \in \{1, 2\}$ ,  $j \neq k$ , respectively. To derive a model, which is consistent with our experimental configuration, we superimpose a diagonal (reflective) target matrix  $S_*$  on a purely transmissive background  $C$ :

$$S_* = \begin{pmatrix} \sigma + \epsilon & 0 \\ 0 & \sigma - \epsilon \end{pmatrix}, \quad C = \begin{pmatrix} 0 & 1 \\ 1 & 0 \end{pmatrix}, \quad (7)$$

where  $\epsilon$  is the asymmetry and  $\sigma \in \mathbb{R}^+$  is the unitarity factor, which was introduced with the objective of accounting for internal losses. For these prescribed matrices, the nonreciprocal coupling matrix  $D$  is found to be

$$D = \sqrt{\gamma h(\sigma, \epsilon)} \begin{pmatrix} -g(\epsilon) \\ 1 \end{pmatrix}, \quad (8)$$

where  $g(\epsilon) = \epsilon + \sqrt{\epsilon^2 + 1}$  and  $h(\sigma, \epsilon) = (\sigma + \sqrt{\epsilon^2 + 1}) / [g(\epsilon)^2 + 1]$ . The generic nature of our theoretical framework makes this strategy for realizing superradiant scattering applicable not just to the acoustic experiments presented here, but to any system that exhibits nonreciprocal wave-mode coupling and a suitable damping nonlinearity.

For a general model, the nonlinear scattering matrix can be obtained explicitly from the definition  $|s_{\text{out}}\rangle = S|s_{\text{in}}\rangle$  and the Moore-Penrose pseudoinverse:

$$S = \frac{|s_{\text{out}}\rangle \langle s_{\text{in}}|}{\langle s_{\text{in}} | s_{\text{in}} \rangle}. \quad (9)$$

This equation provides an intuitive explanation of why superradiance occurs when waves are scattered at a self-oscillating mode: the energy radiated by the limit cycle  $a_0$  oscillating at a fixed amplitude contributes to the outgoing waves  $|s_{\text{out}}\rangle$  for forcing by the incident wave  $|s_{\text{in}}\rangle$  at a given frequency  $f \approx f_0$ . Even when the forcing is weak, the magnitude of  $|s_{\text{out}}\rangle$  maintains a roughly constant value due to the contribution of  $a \approx a_0$  [see Eq. (3)], which leads the entries of  $S$  to blow up around  $f_0$  as the magnitude of  $|s_{\text{in}}\rangle$  approaches zero. By this argument, sharp peaks in all

the entries of the scattering matrix are expected to occur around  $f_0$  at small forcing amplitudes. We show below that this phenomenon is indeed reproduced by our theory and that it can also be observed in real-world experiments.

To simplify the mathematical steps involved in the derivation of the scattering matrix, we focus on synchronized conditions, which are achievable for small enough detuning and large enough forcing amplitude  $s$  (see Appendix B). For harmonic excitation with angular frequency  $\omega$ , then, we seek the forced response of the nonlinear mode  $a$  as the steady-amplitude solution of Eq. (2) oscillating at the same frequency. By separately applying forcing from each port with  $|s_{\text{in}}\rangle = s|j\rangle e^{i\omega t}$ , using Eq. (9), the nonlinear scattering matrix is found to be

$$S = C + \frac{1}{s} D \sum_{j=1}^2 \rho_j e^{i\varphi_j} |j\rangle \quad (10)$$

$$= \begin{pmatrix} 0 & 1 \\ 1 & 0 \end{pmatrix} + \frac{\sqrt{\gamma h(\sigma, \epsilon)}}{s} \begin{pmatrix} -\rho_1 e^{i\varphi_1} g(\epsilon) & -\rho_2 e^{i\varphi_2} g(\epsilon) \\ \rho_1 e^{i\varphi_1} & \rho_2 e^{i\varphi_2} \end{pmatrix}, \quad (11)$$

where  $a = \rho_j e^{i(\omega t + \varphi_j)}$  is the forced response of  $a$  to incident waves from the  $j$ th port,  $|j\rangle$  is the unit vector in  $j$  direction,  $g(\epsilon) = \epsilon + \sqrt{\epsilon^2 + 1}$  and  $h(\sigma, \epsilon) = (\sigma + \sqrt{\epsilon^2 + 1}) / [g(\epsilon)^2 + 1]$ . The frequency-dependent quantities  $\rho_j \in \mathbb{R}^+$  and  $\varphi_j \in [0, 2\pi)$  follow the modal dynamics (2), and can be determined, for each incident wave frequency  $\omega$ , from the solution of the cubic equation in  $\rho_j$ ,

$$0 = \alpha_0 + \alpha_1 \rho_j^2 + \alpha_2 \rho_j^4 + \alpha_3 \rho_j^6, \quad (12)$$

whose coefficients are derived in Appendix B. Equation (12) has a single real root at all frequencies in the parameter range considered in this work. This solution  $\rho_j$ , which can be obtained numerically or analytically, can then be substituted into the linearly stable branch of  $\varphi_j$ ,

$$\varphi_j = -\arg D_j + \arcsin \left( \frac{\Delta \rho_j}{|D_j| s} \right), \quad (13)$$

where  $\Delta = \omega_0 - \omega$  is the detuning, to obtain the forced response of  $a$  at a given frequency  $\omega$  and amplitude  $s$  of the incident wave.

For  $s \rightarrow \infty$ , the scattering matrix (11) tends to (see Appendix A)

$$S_{s \rightarrow \infty} \approx \begin{pmatrix} \frac{\gamma g(\epsilon)^2 h(\sigma, \epsilon)}{\gamma - i\Delta} & 1 - \frac{\gamma g(\epsilon) h(\sigma, \epsilon)}{\gamma - i\Delta} \\ 1 - \frac{\gamma g(\epsilon) h(\sigma, \epsilon)}{\gamma - i\Delta} & \frac{\gamma h(\sigma, \epsilon)}{\gamma - i\Delta} \end{pmatrix}. \quad (14)$$

In this limit, the intensity reflection coefficient  $|S_{11}|^2$  corresponds to the TCMT result of Fan *et al.*, given by

Eq. (17) of Ref. [32]. For comparison, set  $\{\rho_1, \rho_2, \epsilon, \sigma\} = \{0, 0, 0, 1\}$  in Eq. (11) and  $\{\tau, \phi, t, r\} = \{1/\gamma, -\pi/2, 1, 0\}$  in the reference. As we show in Appendix A, the asymmetry  $\epsilon$  induces a biased gain in the system, which is consistent with the experiments presented below, where a bias is observed due to the presence of a mean flow with non-negligible Mach number in the waveguide. It is worth noting that the present modeling framework is not restricted to the example of 1D reflective scattering considered here and may be extended to different configurations by changing  $S_*$  and  $C$ , as demonstrated on a simple example in Appendix D.

Following Ref. [36], we account for dissipative losses in the linear scattering process at large amplitudes with the internal decay rate  $\gamma_i$ , which is related to the coupling matrix  $D$ :  $D^\dagger D = 2(\gamma - \gamma_i)$ . Combined with Eq. (A6), this formula implies that (see Appendix C)

$$\frac{\gamma_i}{\gamma} = 1 - \frac{\sigma + \sqrt{\epsilon^2 + 1}}{2}. \quad (15)$$

The difference between  $\gamma$  and  $\gamma_i$  is the reversible decay rate  $\gamma_r = \gamma - \gamma_i$ . The nonunitarity and the irreversible losses of the scattering process at large amplitudes are intrinsically connected. In particular, in this limit, unitary scattering ( $\sigma = 1, \epsilon = 0$ ) corresponds to perfect reversibility ( $\gamma = \gamma_r$ ). From a physical perspective, for the superradiant acoustic meta-atom modeled here,  $\gamma_r$  represents radiation losses through the ports and  $\gamma_i$  viscothermal losses along the internal walls of the cavity.

We now focus on the distribution of energy of the scattered waves in the ports. Here, we are referring to “energy” in a generic sense as the squared Euclidian norm of a wave. For a detailed discussion of acoustic energy and scattering in the presence of mean flow, see Ref. [61]. We define the absorption coefficients for incident waves from the  $j$ th port as  $\alpha_j = 1 - \mathcal{R}_{j \rightarrow j}^2 - \mathcal{T}_{j \rightarrow k}^2, j = 1, 2 \neq k$ . Superradiant scattering is defined as  $\alpha_j < 0$ , implying a net amplification of the incident wave energy:  $\langle s_{\text{out}} | s_{\text{out}} \rangle > \langle s_{\text{in}} | s_{\text{in}} \rangle$ .

A numerical example of the theoretically derived scattering matrix Eq. (11) is shown in Fig. 3 as a function of the incident wave frequency  $f = \omega/2\pi$  and the normalized incident wave amplitude  $\tilde{s} = s/\sqrt{\gamma}|a_0|$  [62]. These results were obtained by repeatedly solving Eqs. (12) and (13) for different combinations of  $f$  and  $s$ . Both absorption coefficients are negative over a continuous range of amplitudes and frequencies, indicating a net gain resulting from the contribution of the energy radiated from of the self-sustained limit cycle  $a$ . Because this limit cycle couples nonreciprocally to the outgoing waves, as  $\tilde{s}$  is increased, the scattering matrix undergoes a nonlinear transition from omnidirectional to unidirectional (purely reflective) superradiant scattering. While the change of the transmission

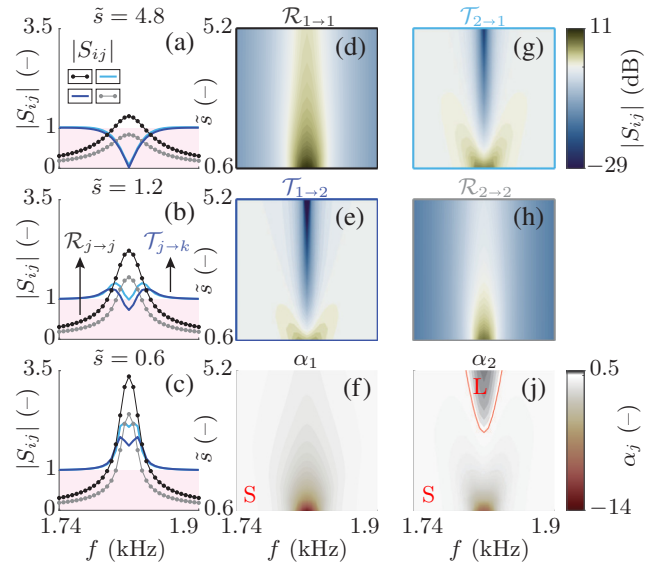


FIG. 3. Theoretical scattering matrix  $S$  of a two-port cavity with a limit cycle at frequency  $f_0 = 1.82$  kHz. The diagonal and off-diagonal elements of  $S$  are reflection ( $|S_{ij}| = \mathcal{R}_{j \rightarrow j}$ ) and transmission ( $|S_{ij}| = \mathcal{T}_{j \rightarrow k}$ ) coefficients, respectively. In this numerical example, we set  $\beta = 172$  rad/s,  $\gamma = 137$  rad/s,  $\sigma = 0.8$ ,  $\epsilon = 0.25$  and  $\kappa = 1$ . Shown are (a)–(c) the scattering matrix coefficients  $|S_{ij}|$  over the incident wave frequency  $f$  and (d)–(j) the same quantities as well as the absorption coefficients  $\alpha_{1,2}$  over  $f$  and the normalized incident wave amplitude  $\tilde{s} = s/\sqrt{\gamma}|a_0|$ . The colors of (d),(e),(g),(h) correspond to the colors of the respective curves in (a)–(c). The interval  $[0, 1]$  in (a)–(c) is colored in red. The red curve in (j) marks the  $\alpha_2 = 0$  contour, separating the domains of superradiant (S) and lossy (L) scattering.

and reflection coefficients over the incident wave amplitude  $\tilde{s}$  is sharp at small amplitudes, at larger amplitudes, a saturation occurs and the superradiance persists with little change.

### III. EXPERIMENTAL VALIDATION

#### A. Superradiant acoustic meta-atom

To validate our theoretical analysis, a superradiant acoustic meta-atom was experimentally realized to achieve a nonlinear cavity mode with similar characteristics as the mode  $a$  in the model presented in II. Deep-cavity whistling was obtained by imposing a low-Mach air flow in the waveguide with a bulk velocity  $U$  that exceeds the threshold of a supercritical Hopf bifurcation. The corresponding aeroacoustic limit cycle at  $f_0 = 1.82$  kHz involves a longitudinal mode of the cavity, which constructively interacts with the coherent vorticity fluctuations in the cavity opening [49–54]. The experimental setup, shown in Fig. 4(a), consists of a square cross-section wind channel with side length  $H = 6.2$  cm and wall thickness equal to 0.4 cm. The channel terminates upstream and downstream in two large

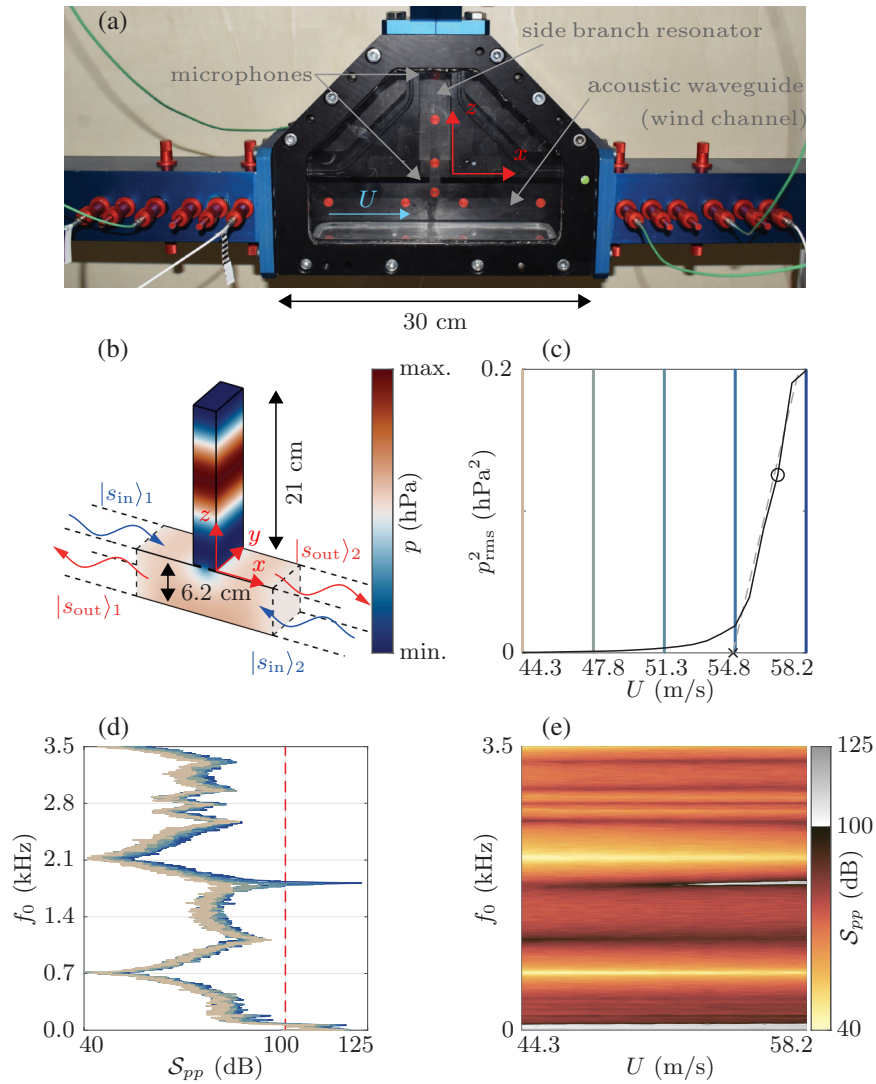


FIG. 4. Acoustic properties of a superradiant acoustic meta-atom in the absence of external forcing ( $|s_{in}| = 0$ ). (a) Experimental setup, consisting of a cavity (side branch resonator) attached to a waveguide (wind channel). An air stream with bulk velocity  $U$  is imposed in the waveguide to create an aeroacoustic limit cycle in the cavity. Microphones were flush mounted in the cavity and in the waveguide for acoustic measurements. (b) Acoustic eigenmode of the cavity-waveguide system at  $f = 1.82$  kHz. (c) Squared rms amplitude of the bandpass-filtered acoustic pressure between 1.74 and 1.9 kHz inside the cavity, showing the bifurcation point at  $U = 54.8$  m/s [ $\times$ ] and the operating point at  $U = 56.8$  m/s [ $\circ$ ], superimposed on a regression line (gray, dashed). (d) PSD  $\mathcal{S}_{pp}$  of the acoustic pressure inside the cavity for equally spaced values of the bulk flow velocity  $U$ . The value of  $U$  for each of the spectra is indicated by the curves' colors, which correspond to those of the vertical lines in Fig. 4(c). (e) PSD  $\mathcal{S}_{pp}$  of the acoustic pressure  $p$  inside the cavity as a function of the bulk flow speed  $U$ .

anechoic ends (not shown), which were measured to reflect less than 2% of acoustic energy in the frequency range of interest for all considered operating conditions. See Fig. 1 of Ref. [53] for a sketch of the anechoic ends. A steadily operated blower allows us to impose a low Mach mean flow in this acoustic waveguide. The bulk velocity  $U$  is deduced from the mass flow and the temperature in the channel, which are measured with a Bronkhorst IN-FLOW F-106CI mass flow meter and a thermocouple. As shown in Fig. 4(a), in the middle of the channel, at  $x_0 = -1.5$  cm,

a rectangular aperture of width  $W = 1$  cm, depth  $H = 6.2$  cm, and length (in  $z$  direction)  $d = 0.2$  cm opens up into a deep rectangular cavity of width  $3W = 3$  cm, depth  $H$ , and length  $L = 21$  cm.

For certain ranges of the bulk flow velocity, whistling occurs due to an aeroacoustic instability, leading to self-sustained shear layer oscillations at the aperture of the side branch cavity. In addition to these unforced, self-sustained oscillations, the system can be subjected to upstream and downstream acoustic forcing with compression drivers

located in the anechoic terminations of the waveguide. For the acoustic measurements, two G.R.A.S. 46BD 1/4" CCP microphones were flush mounted in the center ( $x = x_0$ ) at  $z = -3.1$  and  $z = 9$  cm. The lower of these central microphones was used for calibration of the forcing amplitude and the upper one for measuring the acoustic pressure inside the cavity during the unforced acoustic experiments. Six microphones of the same type were placed in the waveguide at  $x - x_0 = \pm 18.3, \pm 26.8, \text{ and } \pm 32.3$  cm to reconstruct the incident and outgoing waves in the waveguide.

The properties of the acoustic meta-atom in the absence of external forcing ( $|s_{\text{in}}| = 0$ ) are characterized in Figs. 4(b)–4(d). Figure 4(b) shows finite-element simulations of the Helmholtz equation in the waveguide-cavity system, revealing the structure of the pure acoustic eigenmode (resonance) involved in the aeroacoustic instability considered in this work. The simulations were carried out in MATLAB using the function `solvepdeeig` with default settings on the Helmholtz equation  $\nabla^2 p - (\omega_0/c)^2 p = 0$ , where  $p$  is the acoustic pressure,  $\omega_0$  is the angular eigenfrequency of the resonance and  $c = 344$  m/s is the speed of sound. The domain geometry was generated with CAD software. The boundary conditions set were of Dirichlet type (“open,”  $p = 0$ ) at the upstream and downstream ends of the modeled channel segment ( $x - x_0 = \pm 9$  cm) and of Neumann type (“hard walls,” vanishing wall-normal gradient  $\nabla_{\perp} p = 0$ ) everywhere else. These FEM simulations confirm the existence of a spatially localized resonance, close to the five-quarter mode of a idealized opened-closed cavity, with frequency  $f = 5c/4(L + l) = 1.82$  kHz, where the end correction  $l$  is equal to about 2.7 cm. The trapped mode in the side branch shown in Fig. 4(b) is the acoustic mode that, in the classic scenario of deep-cavity whistling, coherently interacts with the “hydrodynamic,” incompressible shear layer in the cavity aperture to lead to an aeroacoustic limit cycle.

The occurrence of a supercritical Hopf bifurcation is confirmed in Fig. 4(c) by plotting  $p_{\text{rms}}^2$  over  $U$ , where  $p_{\text{rms}}$  is the rms amplitude of the bandpass-filtered acoustic pressure between 1.74 and 1.9 kHz. The dependence of the squared rms amplitude is linear, as expected by the idealized Stuart-Landau theory. By extrapolating a least-squares regression line, the gray dashed line in Fig. 4(c), over the linear region, the bifurcation point, marked by a cross, is estimated to lie at approximately 54.8 m/s. The operating point was defined at  $U = 56.8$  m/s, and is marked by a circle in Fig. 4(c).

Figure 4(d) shows the power spectral density (PSD) of the acoustic pressure inside the cavity for equally spaced values of the bulk flow velocity  $U$ . The value of  $U$  for each of the spectra is indicated by the curves’ colors, which correspond to those of the vertical lines in Fig. 4(c). The flow velocity range encompasses the bifurcation where a linearly stable aeroacoustic mode oscillating at 1.82 kHz

becomes linearly unstable, which leads to a dominant aeroacoustic limit cycle. Indeed, when the flow speed is increased from 50 to 58 m/s, a sharp rise in the acoustic pressure amplitude at this frequency is observed. This peak is narrow and strongly isolated between 1.4 and 2.1 kHz, justifying the 1D nature of the theoretical model in Sec. II. The low-frequency signature of turbulent noise is also visible for  $f_0 \leq 200$  Hz in Fig. 4(d), as for the configuration investigated in Ref. [53]. In the narrow frequency range around 1.82 kHz, at the chosen operating point, coherent effects dominate, as can be seen from Fig. 4(d). Therefore, in that frequency band, the effect of the turbulent, quasistochastic forcing on the nonlinear cavity mode  $a$  can be neglected to reasonable accuracy. Nevertheless, it would be an interesting topic for future research to also include noise in the nonlinear scattering theory; see also the discussion in Sec. IV.

Figure 4(e) shows the PSD of the acoustic pressure in the side cavity for a continuous range of bulk flow velocities. The dark lines in the PSD correspond to several acoustic resonances of the cavity. They are horizontal, which shows that the aeroacoustic feedback does not significantly affect the frequency of the modes.

The operating conditions considered in this work are  $U = 0$  m/s and  $U = 56.8$  m/s. At the latter bulk velocity, due to the non-negligible Mach number  $\text{Ma} \approx 0.17$ , the self-sustained aeroacoustic mode radiates into the upstream and downstream parts of the waveguide in an biased fashion. This leads to a broken symmetry of the system when  $U$  is not negligible compared to the speed of sound  $c \approx 345$  m/s.

Consequently, as a byproduct of this air stream in the waveguide, a bias on the order of  $\text{Ma}$  is imposed on the acoustic system. The measured rms amplitudes of the self-sustained acoustic waves radiated into the upstream and downstream sections of the waveguide at  $x - x_0 = \mp 32.3$  cm were 0.54 and 0.65 hPa, respectively. The acoustic energy of the limit cycle feeds the scattered waves, enabling superradiance in the presence of incident waves.

To measure the scattering matrix  $S$ , acoustic waves produced by two Beyma CP850Nd compression drivers placed in the anechoic ends of the waveguide are sent to the cavity. The presence of these devices does not alter the nonreflective nature of the waveguide terminations. The columns  $S_{i1}$  and  $S_{i2}$ ,  $i = 1, 2$  are obtained separately by applying harmonic forcing upstream and downstream of the cavity. The voltage of the signal to the drivers is calibrated at each frequency to achieve a specified acoustic forcing amplitude  $s$  in the waveguide just outside the cavity aperture. Assuming lossless transmission in the 1D waveguide, the multimicrophone method is employed to reconstruct the forward- and backward-propagating waves in the waveguide [63]. The scattering experiments were repeated 3 times at each operating condition over the considered frequency range to ensure the reproducibility of the

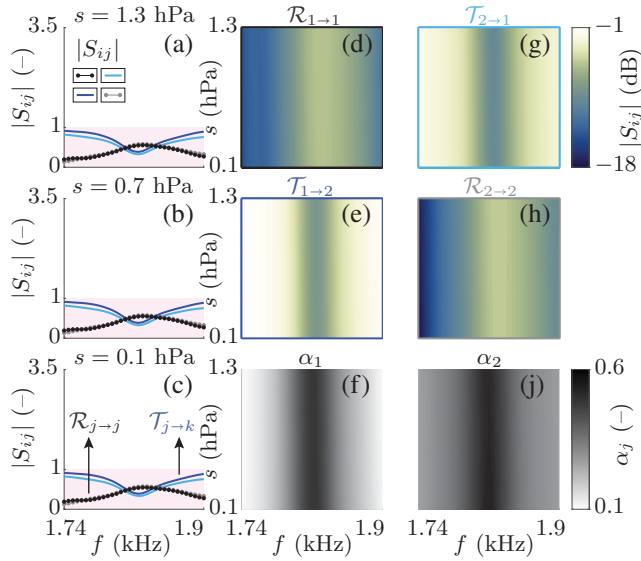


FIG. 5. Experimentally determined scattering matrix of the unbiased resonant cavity depicted in Fig. 4(a) in the absence of air flow ( $U = 0$ ). Shown are the same quantities as in Fig. 3. To measure  $S$ , acoustic forcing at frequency  $f$  with amplitude  $s$  is applied from the upstream and downstream ends of the waveguide.

results. We note that the wavelength  $c/f \geq 20$  cm of the acoustic forcing imposed by the compression drivers significantly exceeds the extensions of the waveguide’s cross section, justifying the 1D plane-wave assumption of the multimicrophone method.

### B. Unbiased case

Before performing the nonlinear scattering experiments, we characterized the scatterer shown in Fig. 4(a) in the absence of an air stream in the waveguide, in which case it acts simply as a resonant side cavity. Figure 5 shows the reflection and transmission coefficients of this unbiased system, i.e., at  $U = 0$  m/s. We observe that the measured scattering matrix is amplitude independent, quasisymmetric, and lossy over the entire range of frequencies and forcing amplitudes considered. These results demonstrate that the nonlinear features discussed in this work are solely caused by the whistling phenomenon induced by the air flow.

### C. Nonlinear scattering experiments

We now present nonlinear scattering experiments performed on a superradiant acoustic meta-atom. Measurements were done for varying incident wave amplitudes  $s$  at the bulk flow velocity  $U = 56.8$  m/s where the side cavity shown in Fig. 4(a) exhibits a limit cycle at  $f_0 = 1.82$  kHz. The experimentally determined nonlinear scattering matrix, shown in Fig. 6, is in excellent qualitative agreement with the theoretical results shown in Fig. 3.

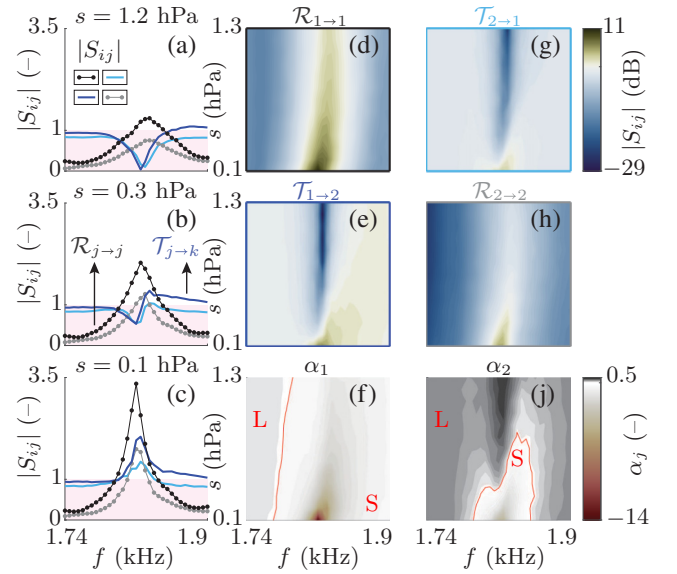


FIG. 6. Experimentally measured scattering matrix of a superradiant acoustic meta-atom in a biased 1D waveguide based on an aeroacoustic limit cycle with eigenfrequency at  $f_0 = 1.82$  kHz. Shown are the same quantities as in Fig. 3. To obtain  $S$ , acoustic forcing at frequency  $f$  with amplitude  $s$  is applied from the two anechoic ends of the waveguide. The rms amplitudes of the acoustic waves radiated by the cavity whistling in the absence of acoustic forcing are 0.54 and 0.65 hPa in the upstream and downstream sections of the waveguide.

As in this numerical example, the experimental scattering matrix exhibits a nonlinear transition with increasing  $s$  from omnidirectional to unidirectional (purely reflective) superradiant scattering. It is interesting to note that in the present biased system, superradiant reflection is stronger for incident waves in flow direction and persists at large forcing amplitudes, confirming its theoretically predicted robustness. At 1825 Hz and  $s = 1.2$  hPa [Fig. 6(a)], the wave reflected back into port “1” experiences an amplitude gain of 20% while less than one per thousand of acoustic energy is transmitted to port “2.” We note that Fig. 6(b) differs qualitatively from the corresponding theoretical results shown in Fig. 3(b). In the future, one may add a Duffing-type nonlinearity in the modal dynamics to obtain reflection and transmission coefficients whose absolute values are not symmetric with respect to reflection around  $f = f_0$ . Alternatively, one could consider a separate model for synchronization instead of always assuming synchronized conditions. The stability domain of the synchronized state will generally not be symmetric with respect to  $f_0$  [64].

## IV. DISCUSSION

The resonant scattering matrix of the cavity without air flow reported in Fig. 5 manifests itself near the resonance frequency  $f_0 = 1.82$  kHz by higher reflection and lower



transmission. It is interesting to note that the superradiant scattering matrix of the acoustic meta-atom shows the same tendency at large forcing amplitudes (see Fig. 6). This enhancement of the resonant scattering matrix, further emphasized in Fig. 7, is explained by the nonlinear coupled-mode theory presented above. The observed behavior also depends on the nonlinear damping force  $F_d$  of a given system. We have not, in this work, investigated the tunability of the system by continuously varying the bifurcation parameter (bulk flow velocity  $U$ ). This topic is part of our ongoing research, which seeks to study theoretically and experimentally if, given an operating condition at which a limit cycle  $a_0$  exists, the desired superradiant scattering state can always be reached by continuously varying the incident wave amplitude  $s$ .

We studied both small-amplitude amplification by a supercritical Hopf bifurcation [65,66] [see Figs. 3(c), 5(c), and 6(c)] as well as scattering for larger forcing amplitudes [see Figs. 3(a), 5(a), and 6(a)]. Our tunable concept is based on the synchronization between incident waves and the radiation losses of a self-oscillating source. As in the nonlocal active metamaterial proposed in Ref. [67], destructive interferences between traveling waves in the absence of the source and waves radiated from the source enable tailoring the scattering to quasiperfect isolation. At the operating condition shown in Fig. 4 (right inset), the scatterer is a reflection amplifier for waves originating from port “1” [68,69]. The inherent directionality of the amplification mechanism discussed here makes it a viable candidate for future use in flow-based acoustic metamaterials [46,60,70,71], which often suffer from dissipation losses.

The self-sustained aeroacoustic system considered in this work can be compared to an electromagnetic circuit with a negative resistance element, such as a Gunn diode [72,73] or a tunnel diode [74–76], except that the negative resistance in our case does not come from an external element but from the aeroacoustic instability, which is

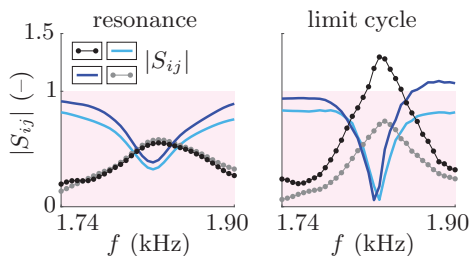


FIG. 7. Experimentally determined scattering matrix coefficients  $|S_{ij}|$  at forcing amplitude  $s = 1.3$  hPa for resonance-based (left inset) and limit-cycle-enhanced scattering (right inset). The black and gray curves correspond to the reflection coefficients  $\mathcal{R}_{1 \rightarrow 1}$  and  $\mathcal{R}_{2 \rightarrow 2}$ , and the blue and cyan curves to the transmission coefficients  $\mathcal{T}_{2 \rightarrow 1}$  and  $\mathcal{T}_{1 \rightarrow 2}$ , respectively. The interval  $[0, 1]$  is colored in red.

intrinsic to the medium that the waves travel in. Our work differs from other recent approaches to unidirectionally amplifying acoustic diodes in that our proposed superradiant meta-atom is all acoustic, without the need for any internal electrical components to manipulate the sound field [77–79]. It would be interesting to attempt to relate the theoretical and experimental results presented above to theoretical results on lasers [80], whose functional principle is also based on selecting a cavity mode and enhancing it using a nonlinear feedback mechanism.

Future applications of our theory may include modeling of optical scatterers, such as complex nonreciprocal devices [69,81,82] and spherical cavities [83]. While the derivation of the background could be performed by choosing suitable matrices  $S_*$  and  $C$  and proceeding in analogy to Appendix A, nonlinearities [84–88], negative feedback [89], or thermal noise [90] may be included through the modal equation(s). To be clear, we do not claim to be able to model, as of now, any of the systems cited above, but we mention them because they feature hallmarks of dynamical systems, which could be included in the nonlinear scattering framework presented in Sec. II. Once the modal equation(s) for  $\hat{a}$  and the equation for  $|s_{\text{out}}|$  have been found, the scattering matrix follows directly from the general expression in Eq. (9).

## V. CONCLUSIONS

In summary, this work shows the following:

- (a) A nonlinear cavity mode undergoing a limit cycle can enable superradiant scattering, whereby incident waves are amplified in one direction and canceled in the opposite direction.
- (b) The above effect is purely dynamic and can be described by a generic nonlinear coupled-mode theory. In this framework, superradiance can arise from synchronization between a limit cycle and an incident wave.
- (c) Aeroacoustic instabilities in deep cavities can be used to experimentally demonstrate superradiant scattering by a limit cycle, showing excellent agreement with theory.

## ACKNOWLEDGMENT

This project is funded by the Swiss National Science Foundation under Grant Agreement 184617.

## APPENDIX A: SCATTERING MATRIX DERIVATION

Since  $C$  was defined *a priori*, the nonlinear scattering matrix in Eq. (11) is determined only by the unknown coupling matrix  $D$ . To derive  $D$  from  $S_*$  and  $C$  [see Eq. (7)], we consider the large amplitude limit of the nonlinear scattering process, given by the TCMT Eqs. (4) and (5). For harmonic forcing with angular frequency  $\omega$ , in

the steady state,  $\dot{a} = i\omega a$ , which leads to  $a = F^{-1}D^\dagger|s_{\text{in}}\rangle$ , where  $F = i(\omega - \omega_0) + \gamma$ . Substituting this intermediate result into Eq. (5) yields the scattering matrix at large amplitudes  $|a| \gg |a_0|$ :

$$|s_{\text{out}}\rangle = (C + DF^{-1}D^\dagger)|s_{\text{in}}\rangle, \quad (\text{A1})$$

where  $C + DF^{-1}D^\dagger$  is the large amplitude scattering matrix. Formally approximating  $S_*$  with this matrix yields a low-rank approximation problem from which the unknown coupling matrix  $D$  can be determined:

$$S_* - C \approx DF^{-1}D^\dagger. \quad (\text{A2})$$

The matrix  $S_* - C$ , where  $S_*$  and  $C$  are defined in the main text, has the following eigenvalues  $\mu_j$  and corresponding normalized eigenvectors  $v_j, j = 1, 2$ :

$$\mu_1 = \sigma + \sqrt{\epsilon^2 + 1}, \quad v_1 = \begin{pmatrix} \frac{-\epsilon - \sqrt{\epsilon^2 + 1}}{\sqrt{(\epsilon + \sqrt{\epsilon^2 + 1})^2 + 1}} \\ [(\epsilon + \sqrt{\epsilon^2 + 1})^2 + 1]^{-1/2} \end{pmatrix}, \quad (\text{A3})$$

$$\mu_2 = \sigma - \sqrt{\epsilon^2 + 1}, \quad v_2 = \begin{pmatrix} \frac{-\epsilon + \sqrt{\epsilon^2 + 1}}{\sqrt{(\epsilon - \sqrt{\epsilon^2 + 1})^2 + 1}} \\ [(\epsilon - \sqrt{\epsilon^2 + 1})^2 + 1]^{-1/2} \end{pmatrix}. \quad (\text{A4})$$

To capture the main characteristics of the specified matrices  $S_*$  and  $C$ , we define the coupling matrix  $D$  such that for resonant forcing ( $F = \gamma$ ), the singular matrix  $DF^{-1}D^\dagger$  shares with  $S_* - C$  its dominant subspectrum, i.e., the eigenvalue with the largest absolute value and the corresponding eigenvector. Both  $D$  as well as the ideal parameter configuration, which we call ‘‘perfect matching,’’ are defined by the following two consistency conditions: (I) The spectrum of the singular matrix  $D\gamma^{-1}D^\dagger$  must coincide with the dominant subspectrum of  $S_* - C$ . (II) For a perfectly matched scatterer with  $\sigma = 1$ ,  $C + D\gamma^{-1}D^\dagger = S_*$  must be unitary.

By the Hermiticity of the chosen  $S_*$  and  $C$ , we can expand the 2-by-2 matrix  $S_* - C$  in terms of its eigenvectors  $v_j \in \mathbb{C}^2$  and eigenvalues  $\mu_j \in \mathbb{R}$  as follows:

$$S_* - C = \mu_1 v_1 v_1^\dagger + \mu_2 v_2 v_2^\dagger, \quad (\text{A5})$$

where  $|\mu_1| \geq |\mu_2|$ . To satisfy (I), we define  $D = v_1 \sqrt{\gamma} \mu_1$ , so that  $D\gamma^{-1}D^\dagger = \mu_1 v_1 v_1^\dagger$ . From (II), we deduce that the perfect matching condition is  $\epsilon = 0$ . Written out, the coupling matrix  $D$  is given by Eq. (8)

$$D = \sqrt{\gamma h(\sigma, \epsilon)} \begin{pmatrix} -g(\epsilon) \\ 1 \end{pmatrix}, \quad (\text{A6})$$

where  $g(\epsilon) = \epsilon + \sqrt{\epsilon^2 + 1}$  and  $h(\sigma, \epsilon) = (\sigma + \sqrt{\epsilon^2 + 1}) / [g(\epsilon)^2 + 1]$ . Written out, the large amplitude limit of the

reflection coefficient of the port ‘‘1’’ at resonant forcing ( $\Delta = 0$ ) is given by

$$S_{11, s \rightarrow \infty} \approx \frac{(\epsilon + \sqrt{\epsilon^2 + 1})^2 (\sigma + \sqrt{\epsilon^2 + 1})}{(\epsilon + \sqrt{\epsilon^2 + 1})^2 + 1}. \quad (\text{A7})$$

For the parameter values used in the numerical example in the main text ( $\sigma = 0.8$  and  $\epsilon = 0.25$ ), we have  $S_{11, s \rightarrow \infty} \approx 1.14$ , showing that the presence of a strong enough asymmetry can lead to biased, reflective superradiance that persists even at large forcing amplitudes.

The spectral low-rank approximation used above is exact when  $\sigma = 1$  and  $\epsilon = 0$ , in which case the spectrum of  $S_* - C$  is singular, and its quality decreases as  $|\mu_1|$  and  $|\mu_2|$  approach each other. In the limiting case  $\sigma = \epsilon = 0$ ,  $S_* - C = -C$  has no distinguished dominant spectral subspace.

## APPENDIX B: FORCED RESPONSE DERIVATION

For simplicity, we write  $\rho_j = \rho$  and  $\varphi_j = \varphi$ . We assume harmonic excitation from the  $j$ th port with  $|s_{\text{in}}\rangle = s|j\rangle e^{i\omega t}$ . Substituting these expressions into the modal dynamics Eq. (2), setting  $\dot{\rho} = \dot{\varphi} = 0$  and separating real and imaginary parts leads to

$$\begin{aligned} & \left[ (|D_j|s)^2 - (\Delta^2 + \gamma^2)\rho^2 \right] (1 + \kappa\rho^2)^2 \\ & + 2\gamma\beta\rho^2(1 + \kappa\rho^2) - \beta^2\rho^2 = 0, \end{aligned} \quad (\text{B1})$$

which can be written as a cubic equation for  $\rho^2$ :

$$0 = \alpha_0 + \alpha_1\rho^2 + \alpha_2\rho^4 + \alpha_3\rho^6, \quad (\text{B2})$$

where

$$\begin{aligned} \alpha_0 &= |D_j|^2 s^2, \\ \alpha_1 &= 2|D_j|^2 s^2 \kappa - (\Delta^2 + \gamma^2) + \beta(2\gamma - \beta), \\ \alpha_2 &= \kappa^2 |D_j|^2 s^2 - 2\kappa(\Delta^2 + \gamma^2) + 2\gamma\beta\kappa, \\ \alpha_3 &= -\kappa^2(\Delta^2 + \gamma^2). \end{aligned}$$

The linearly stable branch of  $\varphi$  is given by [64]

$$\varphi = -\arg D_j + \arcsin\left(\frac{\Delta\rho}{|D_j|s}\right). \quad (\text{B3})$$

This solution can only exist if

$$\left| \frac{\Delta\rho}{|D_j|s} \right| \leq 1, \quad (\text{B4})$$

which is always true for the parameter values considered in this work. Equality in this expression, which would

imply neutral stability of  $\varphi_1$  and  $\varphi_2$ , is never reached here. The inequality Eq. (B4) expresses the well-established notion that synchronization of the forced response with the harmonic excitation is possible only for small enough detuning and large enough forcing amplitude [64].

### APPENDIX C: LOSSES BREAK TIME SYMMETRY

Let us consider here the large amplitude limit of Eqs. (2) and (3), given by the TCMT Eqs. (4) and (5). We model dissipation, or irreversible losses, in this limit using the internal decay rate  $\gamma_i \in \mathbb{R}^+$ . Specifically, following Ref. [36], we assume that the decay rate  $\gamma$  can be decomposed into a part  $\gamma_r$  related to (reversible) decay through the ports and another part  $\gamma_i$  representing irreversible losses:

$$\gamma = \gamma_r + \gamma_i. \quad (\text{C1})$$

The decay through the ports is reversible because the wave energy transmitted in this manner is available to the environment, while the irreversible losses are irrecoverable. For a linear process, the presence of internal losses is marked by a broken time symmetry: while in forward time, the mode  $a$  decays like  $\exp(-\gamma t)$ , its time-reversed counterpart  $a^*$ , where  $(\cdot)^*$  is the complex conjugate, grows like  $\exp(\gamma_r t)$  in backward time, i.e., only the reversible part of the decay rate  $\gamma_r$  contributes to the growth of the time-reversed mode. Following Ref. [36, Eqs. (58) and (59)], the relation between  $\gamma_r$  and the coupling matrix is expressed as follows:

$$\begin{aligned} D^\dagger D &= 2\gamma_r \\ &= 2(\gamma - \gamma_i). \end{aligned} \quad (\text{C2})$$

To confirm the broken time symmetry, we apply a time-reversal transformation to the exponential decay of the mode  $a$  in an initially energized cavity in the absence of forcing, i.e., for  $|s_{\text{in}}\rangle = 0$ . This transformation interchanges  $|s_{\text{in}}\rangle$  and  $|s_{\text{out}}\rangle$  in Eq. (4). In the time-reversed scenario, the mode grows exponentially in backward time with the *a priori* undetermined growth rate  $\tilde{\gamma} \in \mathbb{R}^+$ . The time-reversed dynamics are therefore given by

$$\dot{a}^*(-t) = (i\omega_0 + \tilde{\gamma})a^*(-t) - D^T |s_{\text{out}}\rangle^*(-t), \quad (\text{C3})$$

where  $(\cdot)^*$  is the complex conjugate and  $(\cdot)^T$  is the transpose.

The following steps are analogous to Ref. [33, Sec. II D]. Assuming  $a$  varies in time like  $\exp(i\omega t)$  with complex frequency  $\omega = \omega_0 - i\tilde{\gamma}$ , we have

$$2\tilde{\gamma}a^* = D^T |s_{\text{out}}\rangle^* \quad (\text{C4})$$

$$= D^T (D^* a^*) \quad (\text{C5})$$

$$\Rightarrow D^\dagger D = 2\tilde{\gamma}. \quad (\text{C6})$$

Comparing Eqs. (C2) and (C6) yields

$$\begin{aligned} \tilde{\gamma} &= \gamma - \gamma_i \\ &= \gamma_r, \end{aligned} \quad (\text{C7})$$

demonstrating that time symmetry is broken ( $\gamma \neq \tilde{\gamma}$ ) for  $\gamma_i \neq 0$ . In the case of a linearly stable cavity, using Eq. (C2) and the expression for  $D$  given in the main text, the relation between the internal decay rate  $\gamma_i$ , the unitarity factor  $\sigma$  and the asymmetry  $\epsilon$  given in Eq. (15) is established.

### APPENDIX D: TRANSMISSIVE CASE

Here, to demonstrate the adaptability of our method to different scattering configurations, we derive the coupling matrix  $D$  for a symmetric, purely transmissive target matrix  $S_*$  and a lossless, reflective constant background  $C$  from the TCMT Eqs. (4) and (5):

$$S_* = \begin{pmatrix} 0 & \sigma \\ \sigma & 0 \end{pmatrix}, \quad C = -\begin{pmatrix} 1 & 0 \\ 0 & 1 \end{pmatrix}, \quad (\text{D1})$$

where  $\sigma \in \mathbb{R}^+$  is the unitarity factor. The matrix  $S_* - C$  has the following eigenvalues  $\mu_j$  and corresponding normalized eigenvectors  $v_j, j = 1, 2$ :

$$\mu_1 = 1 - \sigma, \quad v_1 = \frac{1}{\sqrt{2}} \begin{pmatrix} -1 \\ 1 \end{pmatrix}, \quad (\text{D2})$$

$$\mu_2 = \sigma + 1, \quad v_2 = \frac{1}{\sqrt{2}} \begin{pmatrix} 1 \\ 1 \end{pmatrix}. \quad (\text{D3})$$

Note that  $|\mu_2| \geq |\mu_1|$ . To approximate the dominant subspectrum of  $S_* - C$ , we therefore set  $D = v_2 \sqrt{\gamma \mu_2}$ , which leads to the following scattering matrix:

$$\begin{aligned} S &= C + DF^{-1}D^\dagger \\ &= \begin{pmatrix} \frac{\gamma(\sigma+1)}{2(\gamma+i\Delta)} - 1 & \frac{\gamma(\sigma+1)}{2(\gamma+i\Delta)} \\ \frac{\gamma(\sigma+1)}{2(\gamma+i\Delta)} & \frac{\gamma(\sigma+1)}{2(\gamma+i\Delta)} - 1 \end{pmatrix}. \end{aligned} \quad (\text{D4})$$

The internal decay rate  $\gamma_i$  describing irreversible losses is given by

$$\frac{\gamma_i}{\gamma} = \frac{1 - \sigma}{2}. \quad (\text{D5})$$

For resonant forcing ( $\Delta = 0$ ), an imperfectly transmissive scattering state is reached, which deviates from  $S_*$  for nonzero dissipation ( $\sigma < 1$ ):

$$S|_{\omega=\omega_0} = \frac{1}{2} \begin{pmatrix} \sigma - 1 & \sigma + 1 \\ \sigma + 1 & \sigma - 1 \end{pmatrix}. \quad (\text{D6})$$

Note that for  $\sigma = 1$  and  $\Delta = 0$ , the linear scattering matrix  $S$  coincides with  $S_*$ . It is left to the interested reader to study the nonlinear extension of this example.

- [1] R. Brito, V. Cardoso, and P. Pani, *Superradiance*, 2nd ed., Lecture Notes in Physics, Vol. VOLUME293 (Springer, 2020), p. XXI.
- [2] J. Bekenstein and M. Schiffer, The many faces of superradiance, *Phys. Rev. D* **58**, 064014 (1998).
- [3] M. Richartz, S. Weinfurter, A. Penner, and W. Unruh, Generalized superradiant scattering, *Phys. Rev. D* **80**, 124016 (2009).
- [4] R. Penrose and R. Floyd, Extraction of rotational energy from a black hole, *Nat. Phys. Sci.* **229**, 177 (1971).
- [5] C. W. Misner, Black hole's superradiance, *Bull. Am. Phys. Soc.* **17**, 472 (1972).
- [6] A. A. Starobinsky, Amplification of waves reflected from a rotating black hole, *Sov. Phys. JETP* **37**, 28 (1973).
- [7] A. A. Starobinsky and S. M. Churilov, Amplification of electromagnetic and gravitational waves scattered by a rotating black hole, *Sov. Phys. JETP* **38**, 1 (1974).
- [8] Y. B. Zel'dovich, Amplification of cylindrical electromagnetic waves reflected from a rotating body, *Sov. Phys. JETP* **35**, 1085 (1972).
- [9] S. Basak and P. Majumdar, "Superresonance" from a rotating acoustic black hole, *Classical Quantum Gravity* **20**, 3907 (2003).
- [10] E. Berti, V. Cardoso, and J. P. S. Lemos, Quasinormal modes and classical wave propagation in analogue black holes, *Phys. Rev. D* **70**, 124006-1 (2004).
- [11] M. Richartz, A. Prain, S. Liberati, and S. Weinfurter, Rotating black holes in a draining bathtub: Superradiant scattering of gravity waves, *Phys. Rev. D* **91**, 124018 (2015).
- [12] V. Cardoso, A. Coutant, M. Richartz, and S. Weinfurter, Detecting Rotational Superradiance in Fluid Laboratories, *Phys. Rev. Lett.* **117**, 271101 (2016).
- [13] F. Federici, C. Cherubini, S. Succi, and M. Tosi, Superradiance from hydrodynamic vortices: A numerical study, *Phys. Rev. A* **73**, 033604 (2006).
- [14] L. Giacomelli and I. Carusotto, Understanding superradiant phenomena with synthetic vector potentials in atomic Bose-Einstein condensates, *Phys. Rev. A* **103**, 043309 (2021).
- [15] L. Giacomelli and I. Carusotto, Spontaneous quantum superradiant emission in atomic Bose-Einstein condensates subject to a synthetic vector potential, *Phys. Rev. A* **104**, 013313 (2021).
- [16] S. Patrick, A. Geelmuyden, S. Erne, C. F. Barenghi, and S. Weinfurter, Quantum vortex instability and black hole superradiance, *Phys. Rev. Res.* **4**, 033117 (2022).
- [17] T. A. S. Cardoso and M. Richartz, Dissipative quantum vortices and superradiant scattering, *Phys. Rev. A* **106**, 063310 (2022).
- [18] C. Gooding, Dynamics landscape for acoustic superradiance: Acoustic vortex beam superradiance, *Philos. Trans. R. Soc. A* **378**, 20200003 (2020).
- [19] C. Gooding, S. Weinfurter, and W. G. Unruh, Superradiant scattering of orbital angular momentum beams, *Phys. Rev. Res.* **3**, 023242 (2021).
- [20] V. Cardoso, R. Brito, and J. L. Rosa, Superradiance in stars, *Phys. Rev. D* **91**, 124026 (2015).
- [21] V. Cardoso, P. Pani, and T.-T. Yu, Superradiance in rotating stars and pulsar-timing constraints on dark photons, *Phys. Rev. D* **95**, 124056 (2017).
- [22] F. V. Day and J. I. McDonald, Axion superradiance in rotating neutron stars, *J. Cosmol. Astropart. Phys.* **2019**, 051 (2019).
- [23] F. Chadha-Day, B. Garbrecht, and J. McDonald, Superradiance in stars: Non-equilibrium approach to damping of fields in stellar media, *J. Cosmol. Astropart. Phys.* **2022**, 008 (2022).
- [24] F. Belgiorno, S. Cacciatori, M. Clerici, V. Gorini, G. Ortenzi, L. Rizzi, E. Rubino, V. Sala, and D. Faccio, Hawking Radiation from Ultrashort Laser Pulse Filaments, *Phys. Rev. Lett.* **105**, 203901 (2010).
- [25] J. Drori, Y. Rosenberg, D. Bermudez, Y. Silberberg, and U. Leonhardt, Observation of Stimulated Hawking Radiation in an Optical Analogue, *Phys. Rev. Lett.* **122**, 010404 (2019).
- [26] M. Cromb, G. Gibson, E. Toninelli, M. Padgett, E. Wright, and D. Faccio, Amplification of waves from a rotating body, *Nat. Phys.* **16**, 1069 (2020).
- [27] D. Acheson, On over-reflexion, *J. Fluid Mech.* **77**, 433 (1976).
- [28] T. Torres, S. Patrick, A. Coutant, M. Richartz, E. Tedford, and S. Weinfurter, Rotational superradiant scattering in a vortex flow, *Nat. Phys.* **13**, 833 (2017).
- [29] J. Steinhauer, Observation of self-amplifying hawking radiation in an analogue black-hole laser, *Nat. Phys.* **10**, 864 (2014).
- [30] J. Steinhauer, Observation of quantum hawking radiation and its entanglement in an analogue black hole, *Nat. Phys.* **12**, 959 (2016).
- [31] J. Muñoz de Nova, K. Golubkov, V. Kolobov, and J. Steinhauer, Observation of thermal hawking radiation and its temperature in an analogue black hole, *Nature* **569**, 688 (2019).
- [32] S. Fan, W. Suh, and J. Joannopoulos, Temporal coupled-mode theory for the Fano resonance in optical resonators, *J. Opt. Soc. Am. A* **20**, 569 (2003).
- [33] W. Suh, Z. Wang, and S. Fan, Temporal coupled-mode theory and the presence of non-orthogonal modes in lossless multimode cavities, *IEEE J. Quantum Electron.* **40**, 1511 (2004).
- [34] Z. Wang and S. Fan, Magneto-optical defects in two-dimensional photonic crystals, *Appl. Phys. B* **81**, 369 (2005).
- [35] V. Dmitriev, G. Portela, and L. Martins, Temporal coupled-mode theory of electromagnetic components described by magnetic groups of symmetry, *IEEE Trans. Microw. Theory Tech.* **66**, 1165 (2018).
- [36] Z. Zhao, C. Guo, and S. Fan, Connection of temporal coupled-mode-theory formalisms for a resonant optical system and its time-reversal conjugate, *Phys. Rev. A* **99**, 033839 (2019).
- [37] L. Carletti, K. Koshelev, C. De Angelis, and Y. Kivshar, Giant Nonlinear Response at the Nanoscale Driven by Bound States in the Continuum, *Phys. Rev. Lett.* **121**, 033903 (2018).
- [38] W. Sweeney, C. Hsu, S. Rotter, and A. Stone, Perfectly Absorbing Exceptional Points and Chiral Absorbers, *Phys. Rev. Lett.* **122**, 093901 (2019).
- [39] C. Gigli, T. Wu, G. Marino, A. Borne, G. Leo, and P. Lalanne, Quasinormal-mode non-hermitian modeling and

- design in nonlinear nano-optics, *ACS Photonics* **7**, 1197 (2020).
- [40] H. Li, A. Mekawy, A. Krasnok, and A. Alù, Virtual Parity-Time Symmetry, *Phys. Rev. Lett.* **124**, 193901 (2020).
- [41] F. Alpeggiani, N. Parappurath, E. Verhagen, and L. Kuipers, Quasinormal-Mode Expansion of the Scattering Matrix, *Phys. Rev. X* **7**, 021035 (2017).
- [42] Y. Mazor, M. Cotrufo, and A. Alù, Unitary Excitation Transfer Between Coupled Cavities using Temporal Switching, *Phys. Rev. Lett.* **127**, 013902 (2021).
- [43] M. Zhang, W. Sweeney, C. Hsu, L. Yang, A. Stone, and L. Jiang, Quantum Noise Theory of Exceptional Point Amplifying Sensors, *Phys. Rev. Lett.* **123**, 180501 (2019).
- [44] S. Franke, J. Ren, M. Richter, A. Knorr, and S. Hughes, Fermi's Golden Rule for Spontaneous Emission in Absorptive and Amplifying Media, *Phys. Rev. Lett.* **127**, 013602 (2021).
- [45] J. Ren, S. Franke, and S. Hughes, Quasinormal Modes, Local Density of States, and Classical Purcell Factors for Coupled Loss-Gain Resonators, *Phys. Rev. X* **11**, 041020 (2021).
- [46] R. Fleury, D. Sounas, C. Sieck, M. Haberman, and A. Alù, Sound isolation and giant linear nonreciprocity in a compact acoustic circulator, *Science* **343**, 516 (2014).
- [47] V. Achilleos, G. Theocharis, O. Richoux, and V. Pagneux, Non-Hermitian acoustic metamaterials: Role of exceptional points in sound absorption, *Phys. Rev. B* **95**, 144303 (2017).
- [48] C. Ferise, P. del Hougne, S. Félix, V. Pagneux, and M. Davy, Exceptional Points of  $pt$ -Symmetric Reflectionless States in Complex Scattering Systems, *Phys. Rev. Lett.* **128**, 203904 (2022).
- [49] D. Rockwell and E. Naudascher, Review-self-sustaining oscillations of flow past cavities, *J. Fluids Eng., Trans. ASME* **100**, 152 (1978).
- [50] M. Howe, The dissipation of sound at an edge, *J. Sound Vib.* **70**, 407 (1980).
- [51] S. Elder, T. Farabee, and F. DeMetz, Mechanisms of flow-excited cavity tones at low Mach number, *J. Acoust. Soc. Am.* **72**, 532 (1982).
- [52] E. Boujo, C. Bourquard, Y. Xiong, and N. Noiray, Processing time-series of randomly forced self-oscillators: The example of beer bottle whistling, *J. Sound Vib.* **464**, 114981 (2020).
- [53] C. Bourquard, A. Faure-Beaulieu, and N. Noiray, Whistling of deep cavities subject to turbulent grazing flow: Intermittently unstable aeroacoustic feedback, *J. Fluid Mech.* **909**, A19 (2020).
- [54] T. Pedergnana, C. Bourquard, A. Faure-Beaulieu, and N. Noiray, Modeling the nonlinear aeroacoustic response of a harmonically forced side branch aperture under turbulent grazing flow, *Phys. Rev. Fluids* **6**, 023903 (2021).
- [55] J. Stuart, On the non-linear mechanics of hydrodynamic stability, *J. Fluid Mech.* **4**, 1 (1958).
- [56] L. D. Landau and E. M. Lifshitz, *Fluid Mechanics* (Pergamon Press Oxford, UK, 1959), Vol. 11.
- [57] V. I. Arnold, *Geometrical Methods in the Theory of Ordinary Differential Equations* (Springer Science & Business Media, New York, NY, 2012), Vol. 250.
- [58] E. Boujo, M. Bauerheim, and N. Noiray, Saturation of a turbulent mixing layer over a cavity: Response to harmonic forcing around mean flows, *J. Fluid Mech.* **853**, 386 (2018).
- [59] P. A. M. Dirac, *The Principles of Quantum Mechanics* (Oxford University Press, Oxford, 1981), Vol. 27.
- [60] Y. Aurégan and V. Pagneux, PT-Symmetric Scattering in Flow Duct Acoustics, *Phys. Rev. Lett.* **118**, 174301 (2017).
- [61] Y. Aurégan and R. Starobinski, Determination of acoustical energy dissipation/production potentiality from the acoustical transfer functions of a multiport, *Acta Acust. United Acust.* **85**, 788 (1999).
- [62] This work uses the scientific color maps of Fabio Cramer described in Ref. [91].
- [63] S.-H. Jang and J.-G. Ih, On the multiple microphone method for measuring in-duct acoustic properties in the presence of mean flow, *J. Acoust. Soc. Am.* **103**, 1520 (1998).
- [64] A. Balanov, N. Janson, D. Postnov, and O. Sosnovtseva, *From Simple to Complex* (Springer, Berlin, Heidelberg, 2009).
- [65] S. Martin and W. Martienssen, Small-signal amplification in the electrical conductivity of barium sodium niobate crystals, *Phys. Rev. A* **34**, 4523 (1986).
- [66] E. Lacot, O. Hugon, and F. Stoeckel, Hopf amplification of frequency-shifted optical feedback, *Phys. Rev. A* **67**, 10 (2003).
- [67] N. Geib, A. Sasmal, Z. Wang, Y. Zhai, B.-I. Popa, and K. Grosh, Tunable nonlocal purely active nonreciprocal acoustic media, *Phys. Rev. B* **103**, 165427 (2021).
- [68] M. Westig and T. Klapwijk, Josephson Parametric Reflection Amplifier with Integrated Directionality, *Phys. Rev. Appl.* **9**, 064010 (2018).
- [69] Q. Zhong, S. Ozdemir, A. Eisfeld, A. Metelmann, and R. El-Ganainy, Exceptional-Point-Based Optical Amplifiers, *Phys. Rev. Appl.* **13**, 014070 (2020).
- [70] S. Cummer, J. Christensen, and A. Alù, Controlling sound with acoustic metamaterials, *Nat. Rev. Mater.* **1**, 16001 (2016).
- [71] Y. Ding, Y. Peng, Y. Zhu, X. Fan, J. Yang, B. Liang, X. Zhu, X. Wan, and J. Cheng, Experimental Demonstration of Acoustic Chern Insulators, *Phys. Rev. Lett.* **122**, 014302 (2019).
- [72] B. Knight and G. Peterson, Theory of the Gunn effect, *Phys. Rev.* **155**, 393 (1967).
- [73] E. Mosekilde, R. Feldberg, C. Knudsen, and M. Hindsholm, Mode locking and spatiotemporal chaos in periodically driven Gunn diodes, *Phys. Rev. B* **41**, 2298 (1990).
- [74] W. Bernard, H. Roth, A. Schmid, and P. Zeldes, Junction potential studies in tunnel diodes, *Phys. Rev.* **131**, 627 (1963).
- [75] H. Nguyen, D. Vishnevsky, C. Sturm, D. Tanese, D. Solnyshkov, E. Galopin, A. Lemaitre, I. Sagnes, A. Amo, G. Malpuech, and J. Bloch, Realization of a Double-Barrier Resonant Tunneling Diode for Cavity Polaritons, *Phys. Rev. Lett.* **110**, 236601 (2013).
- [76] S. Fluckey, S. Tiwari, C. Hinkle, and W. Vandenberghe, Three-Dimensional-Topological-Insulator Tunnel Diodes, *Phys. Rev. Appl.* **18**, 064037 (2022).

- [77] A. Melnikov, Y. Chiang, L. Quan, S. Oberst, A. Alù, S. Marburg, and D. Powell, Acoustic meta-atom with experimentally verified maximum Willis coupling, *Nat. Commun.* **10**, 3148 (2019).
- [78] X. Zhu, J. Li, C. Shen, G. Zhang, S. Cummer, and L. Li, Tunable unidirectional compact acoustic amplifier via space-time modulated membranes, *Phys. Rev. B* **102**, 024309 (2020).
- [79] X. Wen, H. K. Yip, C. Cho, J. Li, and N. Park, Acoustic Amplifying Diode using Nonreciprocal Willis Coupling, *Phys. Rev. Lett.* **130**, 176101 (2023).
- [80] H. Schomerus, K. Frahm, M. Patra, and C. Beenakker, Quantum limit of the laser line width in chaotic cavities and statistics of residues of scattering matrix poles, *Physica A* **278**, 469 (2000).
- [81] W. Śmigaj, L. Magdenko, J. Romero-Vivas, S. Guenneau, B. Dagens, B. Gralak, and M. Vanwolleghem, Compact optical circulator based on a uniformly magnetized ring cavity, *Photonics Nanostruct.: Fundam. Appl.* **10**, 83 (2012).
- [82] X.-W. Xu and Y. Li, Optical nonreciprocity and optomechanical circulator in three-mode optomechanical systems, *Phys. Rev. A* **91**, 053854 (2015).
- [83] H. Xie, L.-W. He, X. Shang, G.-W. Lin, and X.-M. Lin, Nonreciprocal photon blockade in cavity optomagnonics, *Phys. Rev. A* **106**, 053707 (2022).
- [84] M. Stephen Yeung and S. Strogatz, Nonlinear dynamics of a solid-state laser with injection, *Phys. Rev. E* **58**, 4421 (1998).
- [85] S. Roke, M. Bonn, and A. Petukhov, Nonlinear optical scattering: The concept of effective susceptibility, *Phys. Rev. B* **70**, 115106 (2004).
- [86] J.-B. Shim, P. Schlagheck, M. Hentschel, and J. Wiersig, Nonlinear dynamical tunneling of optical whispering gallery modes in the presence of a Kerr nonlinearity, *Phys. Rev. A* **94**, 053849 (2016).
- [87] S. Suwunnarat, Y. Tang, M. Reisner, F. Mortessagne, U. Kuhl, and T. Kottos, Non-linear coherent perfect absorption in the proximity of exceptional points, *Commun. Phys.* **5**, 5 (2022).
- [88] J. Silver and P. Del’Haye, Generalized theory of optical resonator and waveguide modes and their linear and Kerr nonlinear coupling, *Phys. Rev. A* **105**, 023517 (2022).
- [89] R. De Assis, C. Villas-Boas, and N. De Almeida, Negative response with an optical cavity and traveling wave fields, *Phys. Rev. A* **96**, 013821 (2017).
- [90] S. Webster, M. Oxborrow, S. Pugla, J. Millo, and P. Gill, Thermal-noise-limited optical cavity, *Phys. Rev. A* **77**, 033847 (2008).
- [91] F. Cramer, G. Shephard, and P. Heron, The misuse of colour in science communication, *Nat. Commun.* **11**, 5444 (2020).